AUTHOR(S):

Murase, Kohta; Kashiyama, Kazumi; Kiuchi, Kenta; Bartos, Imre

GAMMA-RAY AND HARD X-RAY EMISSION FROM PULSAR-AIDED SUPERNOVAE AS A PROBE OF PARTICLE ACCELERATION IN EMBRYONIC PULSAR WIND NEBULAE

Kohta Murase[1,2,6], Kazumi Kashiyama[2,3,7], Kenta Kiuchi[4], and Imre Bartos[5]

[1] Institute for Advanced Study, Princeton, NJ 08540, USA
[2] Center for Particle and Gravitational Astrophysics, Department of Physics, Department of Astronomy & Astrophysics, Pennsylvania State University, University Park, PA 16802, USA
[3] Department of Astronomy and Theoretical Astrophysics Center, University of California, Berkeley, CA 94720, USA
[4] Yukawa Institute for Theoretical Physics, Kyoto University, Kyoto, Kyoto 606-8502, Japan
[5] Department of Physics, Columbia Astrophysics Laboratory, Columbia University, New York, NY 10027, USA

ABSTRACT

It has been suggested that some classes of luminous supernovae (SNe) and gamma-ray bursts (GRBs) are driven by newborn magnetars. Fast-rotating proto-neutron stars have also been of interest as potential sources of gravitational waves (GWs). We show that for a range of rotation periods and magnetic fields, hard X-rays and GeV gamma rays provide us with a promising probe of pulsar-aided SNe. It is observationally known that young pulsar wind nebulae (PWNe) in the Milky Way are very efficient lepton accelerators. We argue that, if embryonic PWNe satisfy similar conditions at early stages of SNe (in ~1–10 months after the explosion), external inverse-Compton emission via upscatterings of SN photons is naturally expected in the GeV range as well as broadband synchrotron emission. To fully take into account the Klein–Nishina effect and two-photon annihilation process that are important at early times, we perform detailed calculations including electromagnetic cascades. Our results suggest that hard X-ray telescopes such as *NuSTAR* can observe such early PWN emission by follow-up observations in months to years. GeV gamma-rays may also be detected by *Fermi* for nearby SNe, which serve as counterparts of these GW sources. Detecting the signals will give us an interesting probe of particle acceleration at early times of PWNe, as well as clues to driving mechanisms of luminous SNe and GRBs. Since the Bethe–Heitler cross section is lower than the Thomson cross section, gamma rays would allow us to study subphotospheric dissipation. We encourage searches for high-energy emission from nearby SNe, especially SNe Ibc including super-luminous objects.

Key words: gamma-ray burst: general – pulsars: general – radiation: dynamics – radiation mechanisms: non-thermal – supernovae: general

1. INTRODUCTION

Neutron stars (NSs) are left as remnants of core-collapse supernovae (SNe). A proto-NS cools via radiation of MeV neutrinos in the Kelvin–Helmholtz timescale of ~10–100 s, and the neutrino-driven wind forms a hot bubble in the SN cavity. For fast-rotating NSs, their rotation energy is non-negligible and can be larger than the typical SN explosion energy ~10^{51} erg (e.g., Ostriker & Gunn 1971). If NSs are magnetized and can supply enough plasma, it is extracted as the Poynting flux and the spin-down luminosity may contribute to observed SN emission. Interestingly, recent surveys for optical and infrared transients have revealed a diversity of SN phenomena (e.g., Arcavi et al. 2010; Smith et al. 2011; Gal-Yam 2012), and some super-luminous SNe (especially hydrogen-poor SNe) and hypernovae can be explained as pulsar-powered SNe (e.g., Wheeler et al. 2000; Thompson et al. 2004; Kasen & Bildsten 2010; Woosley 2010; Metzger et al. 2011; Inserra et al. 2013; Nicholl et al. 2013; McCrum et al. 2014). Even long gamma-ray bursts (GRBs) may be driven by fast-rotating magnetars with magnetic fields of ~10^{14}–10^{15} G if a proto-NS wind forms relativistic jets (e.g., Usov 1992; Blackman & Yi 1998; Dai & Lu 1998; Zhang & Mészáros 2001; Thompson et al. 2004; Metzger et al. 2011; Murase et al. 2011b), and fast

rotation with spin periods of $P_i \lesssim 3$ ms has been expected in the dynamo scenario (Duncan & Thompson 1992).

On the other hand, regardless of above theoretical expectations, pulsar wind nebulae (PWNe) with ages of $\gtrsim 100$ yr have been observationally established as efficient particle accelerators (Gaensler & Slane 2006). Measurements of the pulsar rotation period P and its derivative $\dot{P}$ lead to the spin-down luminosity. In comparison with multi-wavelength observations, a significant fraction of the spin-down power is dissipated and used for acceleration of relativistic electrons and positrons (Rees & Gunn 1974; Kennel & Coroniti 1984; Atoyan & Aharonian 1996; de Jager et al. 1996; Tanaka & Takahara 2010). Young PWNe such as the Crab Nebula suggest that accelerated leptons typically have TeV energies and radiate synchrotron and inverse-Compton (IC) photons at broad wavelengths. However, particle acceleration mechanisms before or around the termination shock are not well known. In the classical model, the magnetic energy needs to be converted into the kinetic energy (Rees & Gunn 1974; Kennel & Coroniti 1984), but details of magnetic dissipation and related processes such as the kink instability are still under debate (e.g., Begelman 1998; Lyubarsky & Kirk 2001; Arons 2012; Cerutti et al. 2014; Porth et al. 2014).

In this work, we consider implications of such PWNe for early SN emission, focusing on hard X-rays and gamma-ray emission. If embryonic PWNe are efficient lepton accelerators as seen in Galactic PWNe, broadband non-thermal emission should naturally be expected as well (e.g., Verezinskii &

---

[6] Hubble Fellow.
[7] Einstein Fellow.

Prilutskii 1978; Gaisser et al. 1987; Volonteri & Perna 2005; Kotera et al. 2013; Medvedev & Poutanen 2013). In particular, Kotera et al. (2013) recently argued that TeV gamma rays provide promising signals that are detectable by gamma-ray telescopes. Future gamma-ray telescopes such as the Cherenkov Telescope Array (CTA) (Actis et al. 2011) will also be useful. Another interesting signature is predicted at soft X-rays (Metzger et al. 2014), and breakout gamma-ray emission is also expected a bit earlier than breakout optical emission. At early stages, the photon density in a wind bubble is large enough for the two-photon annihilation process and subsequent electromagnetic cascades should occur. The surrounding ejecta density is also quite large, where X-rays and gamma rays are significantly attenuated. Focusing on hard X-rays and gamma rays, we here provide detailed studies of high-energy photon spectra of pulsar-aided SNe,[8] and show that their non-thermal signatures are useful to understand how efficient lepton acceleration begins in PWNe. Driving mechanisms of super-luminous SNe, hypernovae, and GRBs are unknown. Thus, successful detections of such high-energy signals, which support the existence of fast-rotating NSs embedded in stellar material, will help us reveal links between these energetic SNe and ordinary SNe. In addition, proto-NSs have also been considered as promising sources of gravitational waves (GWs) (see reviews, e.g., Kokkotas & Röser 2008; Bartos et al. 2013, and references therein). In particular, if a millisecond pulsar is significantly deformed, a fraction of the rotational energy can be emitted as GWs (e.g., Ostriker & Gunn 1969; Cutler 2002; Stella et al. 2005; Dall'Osso et al. 2009), which is detectable by second-generation ground-based GW interferometers such as Advanced LIGO (Harry & LIGO Scientific Collaboration 2010), Advanced Virgo (Acernese et al. 2014), and KAGRA (Somiya & KAGRA Collaboration 2012).

In Section 2, we describe the basic picture and method of calculation. We also provide analytic spectra, taking into account the Klein–Nishina (KN) effect that is relevant in our problem. We show our numerical results in Section 3. In Section 4, we additionally discuss related issues and then summarize our results.

Throughout this work, we use the notation $Q = 10^x Q_x$ in CGS units unless noted otherwise.

2. BASIC SETUP

2.1. Dynamics

A massive star with $\gtrsim 8\, M_\odot$ has been believed to cause a SN explosion, leaving a proto-NS or black hole. The NS is initially hot, and cools down in the Kelvin–Helmholtz timescale of ~ 10–$100\,\mathrm{s}$. Initially, mass losses are mainly caused by a thermal neutrino-driven wind, and a hot wind-driven bubble forms in the SN cavity. When the NS is rotating and magnetized, its early pulsar wind is expected to become Poynting-dominated and relativistic (e.g., Thompson et al. 2004). Then, as in Galactic PWNe, one may expect that almost all the spin-down power is converted into radiation. The rotation energy budget is

$$\mathcal{E}_{\mathrm{rot},i} = \frac{I\left(2\pi/P_i\right)^2}{2} \simeq 2.8 \times 10^{51}\,\mathrm{erg}\; P_{i,-2.5}^{-2}, \tag{1}$$

where $I \approx 0.35 M_{\mathrm{ns}} R_{\mathrm{ns}}^2 \simeq 1.4 \times 10^{45}\,\mathrm{g\,cm^2}$ is the moment of inertia (Lattimer & Prakash 2001), where $M_{\mathrm{ns}} = 1.4\, M_\odot$ and $R_{\mathrm{ns}} = 12\,\mathrm{km}$ are used. The initial mass-loss rate is governed by the neutrino-driven wind, and then the wind is carried by electrons and/or positrons especially after the proto-NS is transparent to neutrinos. In the late phase, the spin down of the NS is approximated by

$$-\frac{d\mathcal{E}_{\mathrm{rot}}}{dt} = L_{\mathrm{em}} + L_{\mathrm{gw}}, \tag{2}$$

where the electromagnetic spin-down luminosity is

$$L_{\mathrm{em}} \approx \frac{\mu^2 (2\pi/P)^4}{c^3}\left(1 + C\sin^2\chi_\mu\right). \tag{3}$$

Here $\mu \equiv 0.5 B_{\mathrm{dip}} R_{\mathrm{ns}}^3$ is the magnetic moment, $C \sim 1$ is a prefactor suggested from magnetohydrodynamics simulations (Gruzinov 2005; Spitkovsky 2006; Tchekhovskoy et al. 2013), and χ_μ is the angle between the magnetic and rotation axes. Rotating proto-NSs can be unstable to non-axisymmetric deformations, potentially causing strong GW emission via rotation instabilities including dynamical or secular ones, and/or via magnetic distortion (see Kokkotas 2008; Corsi & Mészáros 2009; Bartos et al. 2013, and references therein). For instance, in the quadrupole approximation, the GW luminosity can roughly be estimated to be

$$L_{\mathrm{gw}} \sim \frac{32}{5}\frac{G\left(\epsilon_G I\right)^2 (2\pi/P')^6}{c^5}, \tag{4}$$

ϵ_G is the ellipticity and P' is the pattern period of the elliptical figure. In particular, strong toroidal magnetic fields may make the NS prolate, and the configuration can increase the angle between deformation and rotation axes until they are orthogonal, where the GW emission can be described by the quadrupole emission of a rotating, non-axisymmetric body deformed by internal magnetic fields (e.g., Cutler 2002; Stella et al. 2005; Dall'Osso et al. 2009).

In most cases in which we are interested, L_{em} is dominant, and L_{em} is estimated to be [9]

$$\begin{aligned}
L_{\mathrm{em}} &= L_{\mathrm{em},i}\left(1 + \frac{t}{t_{\mathrm{em}}}\right)^{-2} \\
&\simeq \begin{cases}
8.6 \times 10^{45}\,\mathrm{erg\,s^{-1}}\, P_{i,-2.5}^{-4} B_{\mathrm{dip},14}^2 & (t \lesssim t_{\mathrm{em}}) \\
8.9 \times 10^{42}\,\mathrm{erg\,s^{-1}}\, B_{\mathrm{dip},14}^{-2} t_7^{-2} & (t > t_{\mathrm{em}}).
\end{cases}
\end{aligned} \tag{5}$$

Here the characteristic spin-down time is given by

$$t_{\mathrm{em}} = \frac{P_i^2 I c^3}{4\pi^2 B_{\mathrm{dip},14}^2 R_{\mathrm{ns}}^6} \simeq 3.2 \times 10^5\,\mathrm{s}\; B_{\mathrm{dip},14}^{-2} P_{i,-2.5}^2. \tag{6}$$

The fate of the early PWN depends on various parameters such as the spin-down power and baryon loading. If the spin-

---

[8] Here we consider both cases where spin-down power is dominant (i.e., pulsar-powered SNe) and sub-dominant.

[9] Different expressions of L_{em} lead to different numerical values. When we adopt the conventional magnetic dipole formula, we have $L_{\mathrm{em}} = \frac{4}{9}\frac{\mu^2 (2\pi/P)^4}{c^3}$ (Ostriker & Gunn 1969). In this case, at $t \gg t_{\mathrm{em}}$, we have $L_{\mathrm{em}} \simeq 6.1 \times 10^{47}\,\mathrm{erg\,s^{-1}}\, B_{\mathrm{dip},15}^{-2} I_{45}^2 R_{\mathrm{ns},6}^{-6} t_4^{-2}$ or $4.0 \times 10^{43}\,\mathrm{erg\,s^{-1}}\, B_{\mathrm{dip},14}^{-2} t_7^{-2}$ for $M_{\mathrm{ns}} = 1.4\, M_\odot$ and $R_{\mathrm{ns}} = 12\,\mathrm{km}$ (Murase et al. 2009). Note that magnetic dissipation in the current sheet may reduce L_{em}.
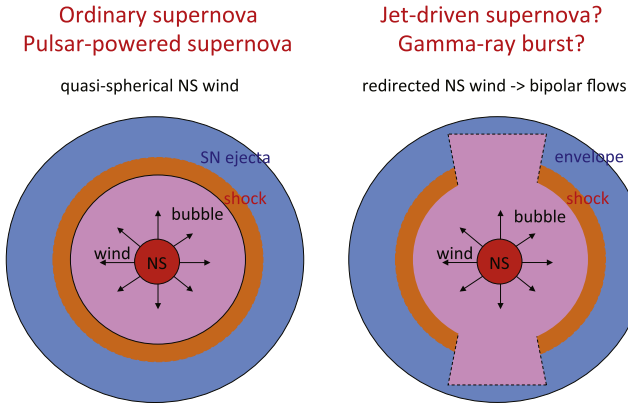
Figure 1. The schematic picture of pulsar-aided SNe. We consider the left case, where a pulsar wind is quasi-spherical and the wind bubble is embedded in the SN ejecta.

down power is high enough, some two-dimensional simulations suggest that the equatorial wind can be redirected by the anisotropic pressure, and hoop stresses lead to bipolar outflows[10] that could explain GRBs (Bucciantini et al. 2007, 2008; Komissarov & Barkov 2007). If not, we expect a quasi-spherical expanding flow embedded in the expanding stellar material (see Figure 1). Assuming a SN explosion with $\mathcal{E}_{sn} \sim 10^{51}$ erg, the SN ejecta expands with its velocity V_{ej} and radius R_{ej}. The early PWN radius R_w also increases non-relativistically, which is given by (e.g., Metzger et al. 2014)

$$\frac{dR_w}{dt} = \sqrt{\frac{7}{6(3-\delta)}\frac{\mathcal{E}_{rot}}{M_{ej}}\left(\frac{R_w}{R_{ej}}\right)^{3-\delta}} + \frac{R_w}{t}, \quad (7)$$

for $R_w < R_{ej}$, otherwise $R_w \approx R_{ej}$ is used. Note that we have used the ejecta density

$$\rho_{ej} = \frac{(3-\delta)M_{ej}}{4\pi R_{ej}^3}\left(\frac{R}{R_{ej}}\right)^{-\delta}, \quad (8)$$

where $\delta \sim 0$–1 is a typical value used in the literature (Kasen & Bildsten 2010; Metzger et al. 2014). The mixture of material allows us to approximate the inner density profile to be reasonably smooth and flat (Chevalier 1977; Chevalier & Fransson 1992). For demonstration, we adopt $\delta = 1$ throughout this work (Kasen & Bildsten 2010; Metzger et al. 2014), and that the radiation pressure is given by $\mathcal{E}_{rot}/(3\mathcal{V}_{nb}) \approx (6/7)\rho_{ej}V_{nb}^2$. Here $\mathcal{V}_{nb}$ is the PWN volume and V_{nb} is the PWN expansion velocity that can be different from V_{ej}. In general, R_w is smaller than R_{ej}, and both of R_{ej} and R_w are numerically determined in this work. Roughly speaking, $R_w \approx R_{ej}$ becomes a good approximation for small values of P such that $\mathcal{E}_{rot,i} \gtrsim \mathcal{E}_{sn}$ (implying $P_i \lesssim 5$ ms $\mathcal{E}_{sn,51}^{-1/2}$). The ejecta velocity V_{ej} and radius R_{ej} can be determined by

$$V_{ej} = \sqrt{\frac{2\left[\int dt\left(\mathcal{E}_{int}/t_{dyn}\right) + \mathcal{E}_{sn}\right]}{M_{ej}}} \quad (9)$$

---

[10] In this case, the (collimated) wind radius is $R_w \approx ct$.

$$\frac{dR_{ej}}{dt} = V_{ej}. \quad (10)$$

The internal energy trapped in the SN ejecta, $\mathcal{E}_{int}$, is given by

$$\frac{d\mathcal{E}_{int}}{dt} = L_{em} - \frac{\mathcal{E}_{int}}{t_{dyn}} - \frac{\mathcal{E}_{int}}{t_{esc}^{ej}}, \quad (11)$$

where $t_{dyn} \approx R_{ej}/V_{ej}$ is the dynamical time. Since X-ray and gamma-ray emission is expected in month-to-year timescales, we only consider energy injection due to L_{em}. In the early phase, as in normal SNe, heating by shocks and unstable isotopes such as ^{56}Ni can be relevant. In the later phase, one may assume that late interactions with circumstellar material are negligible, and injections via the β decay of ^{56}Ni are irrelevant after their lifetime $t_{^{56}Ni} = 6.075$ days $\simeq 5.2 \times 10^5$ s. Visible photons leave the SN ejecta in the escape time

$$t_{esc}^{ej} \approx \frac{\left(1 + \tau_T^{ej}\right)R_{ej}}{c}, \quad (12)$$

where the Thomson optical depth in the ejecta is given by $\tau_T^{ej} \approx K_T \rho_{ej}(R_{ej})R_{ej}$, which is estimated to be

$$\tau_T^{ej} \approx \frac{(3-\delta)K_T M_{ej}}{4\pi R_{ej}^2} \simeq 13\left(2/\mu_e\right)\left(M_{ej}/5\,M_\odot\right)$$
$$\times \left(V_{ej}/5000\text{ km s}^{-1}\right)^{-2}t_7^{-2}, \quad (13)$$

where $K_T = \mu_e^{-1}\sigma_T/m_u$, μ_e is the mean molecular weight per electron, and m_u is the atomic mass unit. See also Equation (45) below. Two of the key parameters, E_{sn} and M_{ej}, can be estimated from the SN peak emission and determination of the ejecta velocity V_{ej} via detailed spectroscopy. Note that the bound–free or bound–bound cross section is much higher at $\lesssim 10$ keV energies, and thermal photons are still generated at later times.

Non-thermal photons generated in the PWN are significantly thermalized in the SN ejecta. Since we are interested in the IC emission, we need to estimate a thermal component, which serves as a seed photon field. Ideally, self-consistent calculations including the detailed radiative transfer are needed. But, for the present purpose, the following approximate approach is sufficient. The internal energy is divided into the thermal energy $\mathcal{E}_{th}$ and non-thermal energy $\mathcal{E}_{nonth}$. Following K. Kashiyama et al. (2015, in preparation), the thermal energy is calculated by

$$\frac{d\mathcal{E}_{th}}{dt} = \int dE_\gamma \frac{\left(1 - \mathcal{A}_{E_\gamma}\right)E_\gamma \mathcal{N}_{E_\gamma}}{t_{esc}^{ej}} - \frac{\mathcal{E}_{th}}{t_{dyn}} - \frac{\mathcal{E}_{th}}{t_{esc}^{ej}}, \quad (14)$$

where $\mathcal{N}_{E_\gamma}$ is the differential photon number (per energy) and $\mathcal{A}_{E_\gamma}$ is the energy-dependent albedo factor, i.e., the fraction of photons escaping without thermalization. In this work, for simplicity, we use $\mathcal{A}_{E_\gamma} = 0.5$ for photon energies below the cutoff due to Compton down-scattering in the SN ejecta, otherwise we set $\mathcal{A}_{E_\gamma} = 0$. Because of the photoelectric absorption (see Section 2.4), soft X-rays and UV photons may not escape until very late times, so our choice is reasonable. Lower values simply imply that more energy is

thermalized, leading to brighter SN emission. Also, in the pulsar-aided SN model, $\mathcal{A}_{E_\gamma}$ can be phenomenologically adjusted to explain observed SN emission (K. Kashiyama et al. 2015, in preparation). Then, the SN temperature is approximated to be $T_{\rm sn} = [\mathcal{E}_{\rm th}/(a\mathcal{V}_{\rm ej})]^{1/4}$, which also gives the photon density of target photons. Here a is the Stefan–Boltzmann constant and $\mathcal{V}_{\rm ej}$ is the volume of the SN ejecta.

Note that interactions in the PWN are negligible in our setup. Assuming the pair multiplicity $\mu_\pm$ is larger than m_p/m_e, the Thomson optical depth in the PWN $(\tau_T^{\rm nb} \approx \sigma_T n_{\rm nb} R_w)$ is estimated to be[11]

$$\tau_T^{\rm nb} \approx \frac{\sigma_T \dot{M}_\pm}{4\pi R_w V_{\rm nb} m_e} \simeq 2.0 \times 10^{-6} \, P_{-2.5}^{-2} B_{\rm dip,14}$$
$$\times \left(\frac{V_{\rm nb}}{5000 \text{ km s}^{-1}}\right)^{-2} t_7^{-1} \mu_{\pm,6}, \tag{15}$$

where the nebula density $n_{\rm nb} \approx \dot{M}_\pm/(4\pi R_w^2 V_{\rm nb} m_e)$ is used and $\dot{M}_\pm$ is the mass-loss rate according to the Goldreich–Julian density multiplied by $\mu_\pm$ (Goldreich & Julian 1969), and P is a function of t.

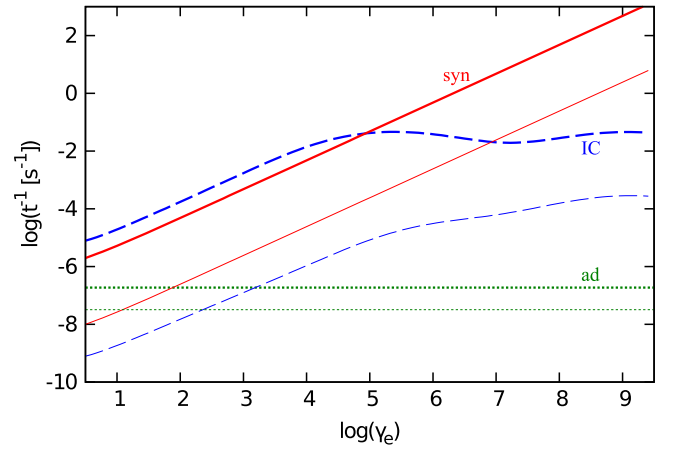### 2.2. Leptonic Emission from Embryonic PWNe

It has been known that Galactic PWNe are efficient accelerators of electrons and positrons. The Crab pulsar is one of the most well-known high-energy gamma-ray sources, and $P_i \approx 19$ ms and $B_{\rm dip} \approx 5 \times 10^{12}$ G are indicated (e.g., Faucher-Giguère & Kaspi 2006). We assume that lepton acceleration can occur even in the very early stage of PWNe similarly to that in Galactic PWNe, and that some extragalactic SNe leave fast-rotating ($P \lesssim 10$ ms) and strongly magnetized ($B_{\rm dip} \gtrsim 10^{13}$ G) NSs. For relativistic leptons, we consider a broken power-law injection spectrum,

$$\frac{d\dot{\mathcal{N}}_e^{\rm inj}}{d\gamma_e} \propto \begin{cases} \gamma_e^{-q_1} & (\gamma_m \leqslant \gamma_e \leqslant \gamma_b) \\ \gamma_e^{-q_2} & (\gamma_b < \gamma_e \leqslant \gamma_M) \end{cases} \tag{16}$$

where $q_1 \, (< 2)$ and $q_2 \, (> 2)$ are low- and high-energy injection spectral indices, and γ_b is the break Lorentz factor. Fitting results on some Galactic PWNe suggest $q_1 \sim 1$–1.5, $q_2 \sim 2.5$–3, $\gamma_b = 10^{4.5}$–10^6, and the significant energy fraction $\epsilon_e \sim 1$ of $L_{\rm em}$ is carried by leptons (Tanaka & Takahara 2010, 2013). The maximum Lorentz factor of accelerated electrons and positrons, γ_M, is given by the balance between the acceleration time and cooling time (see below). The minimum injection Lorentz factor is assumed to be $\gamma_m = 100$ but our results are insensitive to it as long as its value is small enough. In this work, we expect that the wind is largely dominated by pairs so ion acceleration is negligible, where $\mu_\pm$ and γ_b can be related[12] as $\mu_\pm \sim 10^9 \, \epsilon_e \gamma_{b,5}^{-1} (\gamma_b/\gamma_m)^{q_1-1}$ $[(2-q_1)(q_2-2)/(q_1-1)/(q_2-q_1)]B_{\rm dip,14}P_{-2.5}^{-2}$ from number and energy conservation. Details would depend on physics

Figure 2. Cooling timescales of electrons and positrons for $(P_i, B_{\rm dip}, M_{\rm ej})$ $= (2$ ms, 10^{14} G, $5 \, M_\odot)$ at $t = 10^{6.75}$ s $\simeq 65$ days (thick curves) and $t = 10^{7.5}$ s $\simeq 366$ days (thin curves). One can see that relativistic pairs are in the fast cooling regime.

of potential drops and dissipation in the current sheet, where pair production with external photons provided by SN emission plays a role. Note that, for the bulk Lorentz factor Γ_w and the magnetization parameter σ, one also has $\mu_\pm \simeq 1.2 \times 10^{14}[\Gamma_w(1 + \sigma)]^{-1}L_{\rm em,46}^{1/2}$.

Leptons rapidly cool via synchrotron and IC emission mechanisms. In this work, the magnetic field energy density in the early PWN is given by

$$U_B = \epsilon_B \frac{3 \int dt \, L_{\rm em}}{4\pi R_w^3}, \tag{17}$$

where $\epsilon_B = 10^{-3}$–10^{-2} is indicated (e.g., Kennel & Coroniti 1984; Atoyan & Aharonian 1996; de Jager et al. 1996; Tanaka & Takahara 2010). The magnetic field is estimated to be

$$B \simeq 36 \text{ G } P_{i,-2.5}^{-1} \epsilon_{B,-2}^{1/2} \left(\frac{V_{\rm ej}}{5000 \text{ km s}^{-1}}\right)^{-3/2}$$
$$\times t_7^{-3/2}\left[1 - \left(1 + t/t_{\rm em}\right)^{-1}\right]^{1/2}, \tag{18}$$

where $R_w = R_{\rm ej} = V_{\rm ej}t$ is used for analytical estimates.[13] In Figure 2, we plot synchrotron and IC cooling timescales, as well as the dynamical time $t_{\rm dyn} \approx R_{\rm ej}/V_{\rm ej}$. One immediately sees the energy dependence of the synchrotron cooling time $t_{\rm syn} \approx 3m_e c/(4\sigma_T U_B \gamma_e)$, whereas the IC cooling time deviates from the expectation in the Thomson regime, $t_{\rm IC} \propto \gamma_e^{-1}$, due to the KN effect.

The radiative cooling timescale is given by $t_{\rm rad}^{-1} = t_{\rm syn}^{-1} + t_{\rm IC}^{-1} = t_{\rm syn}^{-1}(1 + Y)$, where $Y = t_{\rm syn}/t_{\rm IC}$ is the total Compton Y parameter. Then, at $t \gg t_{\rm em}$, the cooling Lorentz factor of electrons is estimated to be

$$\gamma_c \simeq 1.9 \times 10^{-2} P_{i,-2.5}^2 \epsilon_{B,-2}^{-1} \left(\frac{V_{\rm ej}}{5000 \text{ km s}^{-1}}\right)^3$$
$$\times t_7^2 (1 + Y)^{-1}, \tag{19}$$

---

[11] Note that the Thomson optical depth in the relativistic wind is smaller by a factor of Γ_w^2, so thermalization there is relevant only in the earliest phase.

[12] The pair multiplicity at $t \gg t_{\rm em}$ may not be far from the values obtained for Galactic PWNe. If $\gamma_b > \gamma_M$, acceleration of pairs is limited by strong radiative cooling.

[13] In our numerical calculations, R_w, $R_{\rm ej}$, and $V_{\rm ej}$ are obtained by solving differential equations.

where $t_{\rm rad} = t_{\rm dyn}$ is used. One should keep in mind that γ_e cannot be less than unity physically. If $\gamma_c < 1$ in Equation (19), it simply implies that relativistic electrons will become non-relativistic in $t_{\rm dyn}$ due to strong cooling. Note that, in the Thomson limit, the Y parameter is roughly given by

$$Y \approx \frac{-1 + \frac{L_{\rm sn}t V_{\rm ej}}{\epsilon_B \mathcal{E}_{\rm em}c} + \sqrt{\left(1 + \frac{L_{\rm sn}t V_{\rm ej}}{\epsilon_B \mathcal{E}_{\rm em}c}\right)^2 + \frac{4\epsilon_e L_{\rm em}t V_{\rm ej}}{\epsilon_B \mathcal{E}_{\rm em}c}}}{2}. \quad (20)$$

The distribution of pairs is essentially in the fast cooling regime. In the fast cooling case ($\gamma_c < \gamma_m$) with constant Y, the steady-state electron distribution is $d\mathcal{N}_e/d\gamma_e \propto \gamma_e^{-2}$ for $1 \lesssim \gamma_e \leqslant \gamma_m$, $d\mathcal{N}_e/d\gamma_e \propto \gamma_e^{-q_1-1}$ for $\gamma_m \leqslant \gamma_e \leqslant \gamma_b$ and $d\mathcal{N}_e/d\gamma_e \propto \gamma_e^{-q_2-1}$ for $\gamma_b \leqslant \gamma_e \leqslant \gamma_M$. Using the particle acceleration time $t_{\rm acc} = \eta r_L/c = \eta \gamma_e m_e c^2/eBc$ (where $\eta \geqslant 1$ is the pre-factor accounting for acceleration efficiency), the pair Lorentz factor is limited by

$$\gamma_M \approx \sqrt{\frac{6\pi e \eta^{-1}}{\sigma_T B(1+Y_M)}} \simeq 1.9 \times 10^7\, P_{i,-2.5}^{1/2}\eta^{-1/2}\epsilon_{B,-2}^{-1/4}$$
$$\times \left(\frac{V_{\rm ej}}{5000\ {\rm km\ s^{-1}}}\right)^{3/4} \frac{t_7^{3/4}}{(1+Y_M)^{1/2}}, \quad (21)$$

which is obtained from $t_{\rm acc} = t_{\rm rad}$, and $Y_M \equiv Y(\gamma_M)$ is used. The gamma-ray energy should be lower than

$$E_\gamma^M \approx \gamma_M m_e c^2 \simeq 9.9\ {\rm TeV}\, P_{i,-2.5}^{1/2}\eta^{-1/2}\epsilon_{B,-2}^{-1/4}$$
$$\times \left(\frac{V_{\rm ej}}{5000\ {\rm km\ s^{-1}}}\right)^{3/4}\frac{t_7^{3/4}}{(1+Y_M)^{1/2}}, \quad (22)$$

implying that $\gtrsim$ 10–100 TeV gamma rays are not expected at early stages of the PWN.

In the fast cooling case, the synchrotron photon spectrum is given by

$$E_\gamma L_{E_\gamma}^{\rm syn} \sim \frac{\epsilon_e L_{\rm em}}{2(1+Y)\mathcal{R}_b} \begin{cases} \left(E_\gamma/E_{\rm syn}^b\right)^{(2-q_1)/2} & \left(E_\gamma \leqslant E_{\rm syn}^b\right) \\ \left(E_\gamma/E_{\rm syn}^b\right)^{(2-q_2)/2} & \left(E_{\rm syn}^b \leqslant E_\gamma\right) \end{cases} \quad (23)$$

where $\mathcal{R}_b \sim (2-q_1)^{-1} + (q_2-2)^{-1}$. The characteristic synchrotron energy is given by

$$E_{\rm syn}^b \approx \frac{3}{2}\hbar\gamma_b^2\frac{eB}{m_e c} \simeq 6.3\ {\rm keV}\, \gamma_{b,5}^2 P_{i,-2.5}^{-1}\epsilon_{B,-2}^{1/2}$$
$$\times \left(\frac{V_{\rm ej}}{5000\ {\rm km\ s^{-1}}}\right)^{-3/2} t_7^{-3/2}, \quad (24)$$

so the peak energy is expected in the X-ray range. Note that the synchrotron maximum energy is

$$E_{\rm syn}^M \approx \frac{3}{2}\hbar\gamma_M^2\frac{eB}{m_e c} \approx \hbar\frac{9\pi e^2}{\eta\sigma_T m_e c(1+Y_M)}$$
$$\simeq 240\ {\rm MeV}\, \eta^{-1}(1+Y_M)^{-1}, \quad (25)$$

which hardly depends on various parameters.

The basic process for high-energy gamma-ray emission is the IC mechanism. The expected IC luminosity[14] is very roughly written as $L_{\rm IC} \sim Y(1+Y)^{-1}L_e$. First, let us assume that the seed photon spectrum has $E_\gamma L_{E_\gamma} \propto E_\gamma^{2-\beta}$ with $\beta \lesssim 1 + q_1/2$. Note that the synchrotron self-Compton (SSC) case corresponds to $\beta = 1 + q_1/2$ (in the fast cooling regime). Then, the IC photon spectrum in the Thomson limit is expressed to be

$$E_\gamma L_{E_\gamma}^{\rm IC} \propto \begin{cases} E_\gamma^{(2-q_1)/2} & \left(E_\gamma \leqslant E_{\rm IC}^b\right) \\ E_\gamma^{(2-q_2)/2} & \left(E_{\rm IC}^b < E_\gamma\right). \end{cases} \quad (26)$$

One can obtain the above expression, noting that $L_{E_\gamma}^{\rm IC} \sim \int d\gamma_e(d\tau_{\rm IC}/d\gamma_e)L_E^{\rm seed}(\gamma_e, E)$, where $\gamma_e(d\tau_{\rm IC}/d\gamma_e) \propto \gamma_e^{-q_1}$ for $\gamma_e \leqslant \gamma_b$ and $\gamma_e(d\tau_{\rm IC}/d\gamma_e) \propto \gamma_e^{-q_2}$ for $\gamma_b < \gamma_e$, and $\tau_{\rm IC}$ is the IC optical depth. The similar spectrum is expected in the Thomson limit, when the seed photon spectrum is thermal. In the SSC case, the typical IC energy is

$$E_{\rm SSC}^b \approx 2\gamma_b^2 E_{\rm syn}^b \simeq 130\ {\rm TeV}\, \gamma_{b,5}^4 P_{i,-2.5}^{-1}\epsilon_{B,-2}^{1/2}$$
$$\times \left(\frac{V_{\rm ej}}{5000\ {\rm km\ s^{-1}}}\right)^{-3/2} t_7^{-3/2}, \quad (27)$$

but such high energies are difficult to achieve at early times due to Equation (22). In timescales of days to months, SN emission can be prominent, where thermal photons are upscattered by relativistic pairs via the external IC (EIC) process. The energy flux of seed photons has a peak at $E_{\rm sn} \approx 3.92kT_{\rm sn}$, and the typical IC energy is

$$E_{\rm EIC}^b \approx 2\gamma_b^2 E_{\rm sn} \simeq 78\ {\rm GeV}\, \gamma_{b,5}^2(kT_{\rm sn}/1\ {\rm eV}). \quad (28)$$

Note that Equation (26) can be used for both SSC and EIC cases.

However, the KN effect becomes very important at sufficiently high energies. Let us introduce two characteristic energies (Murase et al. 2011b),

$$E_{\rm KN}^{\rm typ} \approx m_e^2 c^4/(2E_{\rm typ}), \quad (29)$$

$$E_{\rm KN}^b \approx \gamma_b m_e c^2, \quad (30)$$

where $E_{\rm typ}$ is the typical energy of target photons. In the SSC and EIC cases, we expect $E_{\rm typ} \approx E_{\rm syn}^b$ and $E_{\rm typ} \approx E_{\rm sn}$, respectively. In the presence of the KN effect, IC spectra become complicated so we take a numerical approach (see Section 3). However, it is useful to see analytical expressions. First, we consider a seed photon spectrum of $E_\gamma L_{E_\gamma} \propto E_\gamma^{2-\beta}$. Introducing $E_{\rm KN,1}$ as the first break energy due to the KN effect,

---

[14] If $\mathcal{Y}$ is introduced as the ratio of the IC energy flux to the seed photon energy flux, one may write $L_{\rm IC} \sim \min(\mathcal{Y}_{\rm syn}L_{\rm syn}, L_e)$.

for $E_{KN,1} > E_{IC}^b$, we have (e.g., Murase et al. 2010; 2011b)

$$E_\gamma L_{E_\gamma}^{IC} \propto \begin{cases} E_\gamma^{(2-q_1)/2} & (E_\gamma \lesssim E_{IC}^b) \\ E_\gamma^{(2-q_2)/2} & (E_{IC}^b < E_\gamma \lesssim E_{KN,1}) \\ E_\gamma^{\beta-q_2} & (E_{KN,1} \lesssim E_\gamma) \end{cases} \quad (31)$$

where the first KN break is given by

$$E_{KN,1} = E_{KN}^{typ} \simeq 33 \text{ GeV} \left(E_{typ}/4 \text{ eV}\right)^{-1}. \quad (32)$$

The IC emission at $E_\gamma > E_{KN,1}$ is dominated by Thomson scattering between pairs with $\gamma_e \sim E_\gamma/(m_e c^2)$ and seed photons with $E \sim m_e^2 c^4/(2E_\gamma)$.

If the first KN break appears below E_{IC}^b, we obtain[15]

$$E_\gamma L_{E_\gamma}^{IC} \propto \begin{cases} E_\gamma^{(2-q_1)/2} & (E_\gamma \lesssim E_{KN,1}) \\ E_\gamma^{\beta-q_1} & (E_{KN,1} < E_\gamma \lesssim E_{KN,2}) \\ E_\gamma^{\beta-q_2} & (E_{KN,2} \lesssim E_\gamma) \end{cases} \quad (33)$$

where $E_{KN,1} = E_{KN}^{typ}$ and

$$E_{KN,2} = E_{KN}^b \simeq 51 \text{ GeV } \gamma_{b,5} \quad (34)$$

is the second KN break. Note that, if $\beta = 1 + q_1/2$ (as expected in the SSC case), we have

$$E_\gamma L_{E_\gamma}^{IC} \propto \begin{cases} E_\gamma^{(2-q_1)/2} & (E_\gamma \lesssim E_{KN,1}) \\ E_\gamma^{\beta-q_2} & (E_{KN,1} \lesssim E_\gamma) \end{cases} \quad (35)$$

where $E_{KN,1} = E_{KN}^b$. This spectrum can be realized in SSC emission from the early PWN, but the break at $E_{KN,1}$ is significantly smeared out because leptons upscattering photons with E_{typ} do not contribute above E_{KN}^{typ}. We do not consider cases where γ_m and γ_M enter expressions, since we assume that γ_m is sufficiently small and γ_M is sufficiently large.

In our setup, EIC emission due to SN photons is often more important for gamma-ray detections. When the seed photon spectrum is thermal, because the Rayleigh–Jeans spectrum is quite hard, the KN cross section becomes important. For $E_{KN,1} > E_{IC}^b$, we expect

$$E_\gamma L_{E_\gamma}^{IC} \propto \begin{cases} E_\gamma^{(2-q_1)/2} & (E_\gamma \lesssim E_{IC}^b) \\ E_\gamma^{(2-q_2)/2} & (E_{IC}^b < E_\gamma \lesssim E_{KN,1}) \\ E_\gamma^{\beta_{KN}-q_2} & (E_{KN,1} \lesssim E_\gamma) \end{cases} \quad (36)$$

where β_{KN} reflects the logarithmic energy dependence in the KN cross section. For example, in the EIC case, one roughly

expects $E_\gamma^{\beta_{KN}} \propto \ln[2E_\gamma E_{sn}/(m_e^2 c^4)]$. For $E_{KN,1} \lesssim E_{IC}^b$, we have

$$E_\gamma L_{E_\gamma}^{IC} \propto \begin{cases} E_\gamma^{(2-q_1)/2} & (E_\gamma \lesssim E_{KN,1}) \\ E_\gamma^{\beta_{KN}-q_1} & (E_{KN,1} < E_\gamma \lesssim E_{KN,2}) \\ E_\gamma^{\beta_{KN}-q_2} & (E_{KN,2} \lesssim E_\gamma). \end{cases} \quad (37)$$

In the latter case, $E_{KN,1} = E_{KN}^{typ}$ and $E_{KN,2} = E_{KN}^b$. As seen in Section 3, these spectra are typically anticipated for the generated EIC emission from the early PWN.

While we have provided analytical estimates, as presented in Section 3, we perform numerical calculations to show resulting X-ray and gamma-ray spectra. This is because not only the KN effect is relevant but also high-energy gamma rays may not escape from the PWN due to the $\gamma\gamma \to e^+e^-$ process. As a result, as shown in Section 3, detailed numerical spectra may deviate from the above analytical estimates even though they come to a reasonable agreement. In this work, for the intrinsic emission from the PWN, we solve the following kinetic equations:

$$\frac{\partial n_{E_e}^e}{\partial t} = \frac{\partial n_{E_e}^{(\gamma\gamma)}}{\partial t} - \frac{\partial}{\partial E}\left[\left(P_{IC} + P_{syn} + P_{ad}\right)n_{E_e}^e\right] + \dot{n}_{E_e}^{inj},$$

$$\frac{\partial n_{E_\gamma}^\gamma}{\partial t} = -\frac{n_{E_\gamma}^\gamma}{t_{\gamma\gamma}} - \frac{n_{E_\gamma}^\gamma}{t_{esc}^{nb}} + \frac{\partial n_{E_\gamma}^{(IC)}}{\partial t} + \frac{\partial n_{E_\gamma}^{(syn)}}{\partial t}, \quad (38)$$

where

$$t_{\gamma\gamma}^{-1} = \int dE_\gamma \, n_{E_\gamma}^\gamma \int \frac{d\cos\theta}{2} \tilde{c}\sigma_{\gamma\gamma},$$

$$\frac{\partial n_{E_\gamma}^{(IC)}}{\partial t} = \int dE_e \, n_{E_e}^e \int dE_\gamma \, n_{E_\gamma}^\gamma \int \frac{d\cos\theta}{2} \tilde{c}\frac{d\sigma_{IC}}{dE_\gamma},$$

$$\frac{\partial n_{E_e}^{(\gamma\gamma)}}{\partial t} = \frac{1}{2} \int dE_\gamma \, n_{E_\gamma}^\gamma \int dE_\gamma' \, n_{E_\gamma'}^\gamma \int \frac{d\cos\theta}{2} \tilde{c}\frac{d\sigma_{\gamma\gamma}}{dE_e}.$$

Here $\tilde{c} = (1 - \cos\theta)c$ (where θ is the angle between two particles), $t_{\gamma\gamma}$ is the two-photon annihilation time, $t_{esc}^{nb} = R_w/c$ is the photon escape time for the PWN, P_{IC} is the IC energy-loss rate, P_{syn} is the synchrotron energy-loss rate, and P_{ad} is the adiabatic energy-loss rate.[16] To save calculation time, we use the continuous energy-loss approximation for the IC process, and assume $E_e = (E_\gamma + E_\gamma')/2$ for pairs produced by $\gamma\gamma \to e^+e^-$. The pair injection rate $\dot{n}_{E_e}^{inj}$ is determined via Equation (16). For simplicity, we consider a one-zone model, assuming that only freshly accelerated leptons are relevant. We solve the above equations for the constant injection with $\dot{n}_{E_e}^{inj}$. For the initial conditions, we use $n_{E_e}^e = 0$ and $n_{E_\gamma}^\gamma$ is set to a blackbody spectrum with T_{sn}. Resulting high-energy photons are produced by injected non-thermal electrons. The calculation is performed during the dynamical time t_{dyn}, and we essentially obtain steady-state spectra. Energy boundaries are set to 10^{-4} and 10^{16} eV with 400 logarithmic energy bins. The differential luminosity before attenuation, which is related to $\mathcal{N}_{E_\gamma}$, is

---

[15] Equation (23) in Murase et al. (2011b) corresponds to Equation (35), so $\beta_l = 1 + (p - 1)/2$ is assumed.

[16] A factor of $1/2$ is introduced to avoid double counting. But, it is unnecessary in the linear-cascade problem, when projectile and target photon spectra are explicitly separated.

calculated by

$$E_\gamma L_{E_\gamma} = \frac{\left(E_\gamma^2 n_{E_\gamma}\right)\mathcal{V}_w}{t_{\text{esc}}^{\text{nb}}}, \tag{39}$$

which gives observed X-ray and gamma-ray fluxes.

2.3. Two-photon Annihilation in Embryonic PWNe

The SN emission and non-thermal synchrotron emission may prevent high-energy gamma rays from leaving the PWN via $\gamma\gamma \to e^+e^-$. We also take into account the gamma-ray attenuation (and subsequent regeneration) in the PWN. The two-photon annihilation cross section is given by

$$\sigma_{\gamma\gamma} = \frac{3}{16}\sigma_T\left(1 - \beta_{\text{cm}}^2\right)\Big[2\beta_{\text{cm}}\left(\beta_{\text{cm}}^2 - 2\right)$$
$$+ \left(3 - \beta_{\text{cm}}^4\right)\ln\big[\left(1 + \beta_{\text{cm}}\right)/\left(1 - \beta_{\text{cm}}\right)\big]\Big], \tag{40}$$

where $\beta_{\text{cm}} = \sqrt{(1 - 4m_e^2 c^4/S)}$ and S is the Mandelstam variable. For a thermal photon spectrum, using the SN photon density $n_\gamma^{\text{sn}} = 2\zeta(3)(kT_{\text{sn}})^3/(\pi^2\hbar^3 c^3)$, the optical depth to pair production is approximated to be

$$\tau_{\gamma\gamma_{\text{sn}}}^{\text{ej}} \approx \frac{3}{16}\sigma_T n_\gamma^{\text{sn}} R_{\text{ej}}\mathcal{G}\left(x = \frac{m_e^2 c^4}{E_\gamma kT_{\text{sn}}}\right)$$
$$\simeq 2.0 \times 10^4 \left(\frac{kT_{\text{sn}}}{1\text{ eV}}\right)^3\left(\frac{V_{\text{ej}}}{5000\text{ km s}^{-1}}\right)t_7, \tag{41}$$

where the function $\mathcal{G}(x) \equiv \mathcal{F}(x)/\zeta(3)$ and $\mathcal{F}(x)$ is defined in Dermer et al. (2012). In the last expression, we have used $\mathcal{G}(x) \simeq 1$ at

$$E_{\gamma\gamma}^{\text{typ}} \approx \frac{m_e^2 c^4}{2kT_{\text{sn}}} \simeq 130\text{ GeV}\left(\frac{kT_{\text{sn}}}{1\text{ eV}}\right)^{-1}. \tag{42}$$

When non-thermal synchrotron emission provides target photons, for a power-law spectrum with $n_E^{\text{syn}} \propto E^{-\beta}$, the optical depth to pair production in the PWN is estimated to be

$$\tau_{\gamma\gamma_{\text{syn}}}^{\text{nb}} \approx 0.2\sigma_T\left(En_E^{\text{syn}}\right)R_w$$
$$\simeq 3.1 \times 10^{-3}\gamma_{b,5}^{-2}P_{i,-2.5}B_{\text{dip},14}^{-2}\epsilon_{B,-2}^{-1/2}\epsilon_e$$
$$\times \left(\frac{V_{\text{ej}}}{5000\text{ km s}^{-1}}\right)^{1/2}\frac{t_7^{-3/2}}{(1 + Y)}\left(\frac{E_\gamma}{E_{\gamma\gamma}^{\text{typ}}}\right)^{\beta-1}, \tag{43}$$

where $R_w \approx R_{\text{ej}} = V_{\text{ej}}t$ is used for analytical estimates here. The typical energy $E_{\gamma\gamma}^{\text{typ}}$ is given by

$$E_{\gamma\gamma}^{\text{typ}} \approx \frac{m_e^2 c^4}{E_{\text{syn}}^b} \simeq 4.1 \times 10^{-2}\text{ GeV }\gamma_{b,5}^{-2}P_{i,-2.5}\epsilon_{B,-2}^{-1/2}$$
$$\times \left(\frac{V_{\text{ej}}}{5000\text{ km s}^{-1}}\right)^{3/2}t_7^{3/2}. \tag{44}$$

In this work, electromagnetic cascades are calculated for emission generated in the PWN. If $R_w < R_{\text{ej}}$, we take into account the further attenuation by SN photon fields, by multiplying by $e^{-(\tau_{\gamma\gamma}^{\text{ej}} - \tau_{\gamma\gamma}^{\text{nb}})}$.
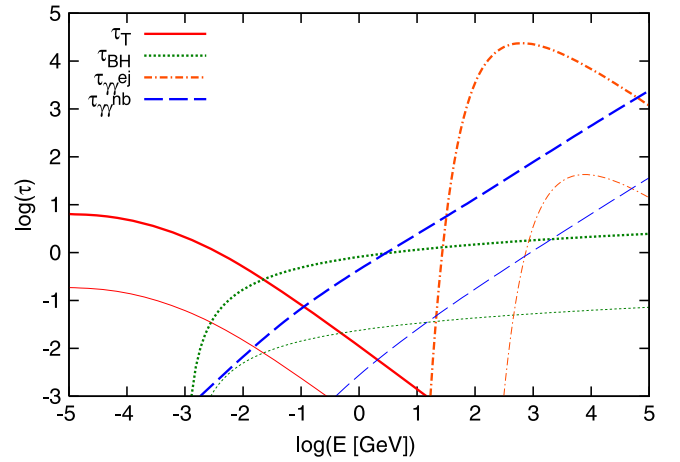
Figure 3. Optical depths to Compton (solid curves), Bethe–Heitler (dotted curves), and two-photon annihilation (dotted–dashed curves for thermal targets; dashed curves for non-thermal targets) processes, for $(P_i, B_{\text{dip}}, M_{\text{ej}})$ = $(2\text{ ms}, 10^{14}\text{ G}, 5\,M_\odot)$. Thick and thin curves are for $t = 10^{6.75}$ s and $t = 10^{7.5}$ s, respectively. One sees that not only SN photons but also synchrotron photons are relevant for two-photon annihilation. Synchrotron photons can prevent multi-GeV gamma rays from leaving the emission.

In Figure 3, we show the optical depth to the two-photon annihilation at different times. One sees that SN photons at optical or infrared bands prevent TeV gamma rays from leaving the PWN. TeV gamma rays are expected to escape from the source in a few years. On the other hand, escape of GeV gamma rays is much more promising but even GeV gamma rays can be strongly attenuated by synchrotron photons for $t \lesssim 30$ days.

2.4. Matter Attenuation in the Stellar Material

Photons escaping from the PWN can be significantly attenuated in the SN ejecta. Although we avoid detailed radiative-transfer calculations, we approximately account for it as a post-process. For photons with energies below ~ 10–30 keV, the most important process is photoelectric absorption. In the soft X-ray band, ionization breakout emission provides an interesting signal from millisecond pulsars embedded in the SN ejecta (Metzger et al. 2014). In this work, we are interested in hard X-rays and gamma rays, which are produced via non-thermal processes, so we mainly focus on Compton scattering and Bethe–Heitler (BH) pair production, which are dominant at high energies. The optical depth is given by $\tau = \tau_{\text{pe}} + \tau_{\text{comp}} + \tau_{\text{BH}}$, where τ_{pe} is the photoelectric absorption optical depth. Using the mass attenuation coefficient K, it is generally expressed to be $\tau \approx K\rho R$, where ρ is the density and R is the size. The photoelectric absorption at high energies is taken into account, using the bound–free opacity $K_{\text{bf}} \simeq 2.37\text{ cm}^2\text{ g}^{-1}(Z/6)^3$ $(E_\gamma/10\text{ keV})^{-3}$ for conservative estimates of X-ray emission.

The Compton optical depth in the ejecta is

$$\tau_{\text{comp}}^{\text{ej}} \approx K_{\text{comp}}\rho_{\text{ej}}R_{\text{ej}} = \frac{(3 - \delta)M_{\text{ej}}\sigma_{\text{comp}}}{4\pi\mu_\ell m_u R_{\text{ej}}^2}, \tag{45}$$

which is reduced to Equation (13) at low energies of $E_\gamma \lesssim 10$ keV, and $K_{\text{comp}} = \sigma_{\text{comp}}/(\mu_\ell m_u)$. The mass energy-transfer

coefficient is obtained using

$$\kappa_{comp}\sigma_{comp} = \frac{3}{4}\sigma_T\left[\frac{2(1+x)^2}{x^2(1+2x)} - \frac{1+3x}{(1+2x)^2}\right.$$
$$- \frac{(1+x)\left(2x^2 - 2x - 1\right)}{x^2(1+2x)^2} - \frac{4x^2}{3(1+2x)^3}$$
$$\left. - \left(\frac{1+x}{x^3} - \frac{1}{2x} + \frac{1}{2x^3}\right)\ln(1+2x)\right], \quad (46)$$

which is obtained from the known KN cross section and kinematics. Here $x \equiv E_\gamma/(m_e c^2)$ and κ_{comp} is the gamma-ray inelasticity.

At high energies, the BH pair production process is dominant. For a nucleus with mass number A and atomic number Z, the BH process on a nucleus scales as $\sigma_{BH} = Z^2\sigma_{BH}^{(p)}$. Taking into account contributions from both nuclei and electrons, for $\mu_e \approx 2$, we have

$$\tau_{BH}^{ej} \approx \frac{(3-\delta)M_{ej}\left(Z_{eff}+1\right)\sigma_{BH}^{(p)}}{8\pi m_u R_{ej}^2}, \quad (47)$$

where Z_{eff} is the effective atomic number, which depends on chemical composition of the ejecta. For $X_H = 0.6$, $X_{He} = 0.3$, and $X_C = 0.1$, we obtain $Z_{eff} \approx 2.5$, while we may have $Z_{eff} \approx 7$ for $X_{CO} = 1$. The mass energy-transfer coefficient at high energies is approximately obtained from

$$\kappa_{BH}\sigma_{BH} = \frac{x-2}{x}\sigma_{BH}, \quad (48)$$

neglecting contributions from electron–positron annihilation. In this work, we use the cross section derived from the Born approximation (Chodorowski et al. 1992). For analytical estimates, one may use a simpler formula

$$\sigma_{BH}^{(p)} \approx \frac{3\alpha}{8\pi}\sigma_T\left[\frac{28}{9}\ln(2x) - \frac{218}{27}\right], \quad (49)$$

which gives $\sigma_{BH} \sim Z^2 10^{-26}$ cm^2 at GeV energies. Note that the BH cross section is of the order of $\sigma_{BH}^{(p)} \sim \alpha_{em}\sigma_T$. At GeV energies, the BH optical depth is estimated by

$$\tau_{BH}^{ej} \simeq 0.57\left([Z_{eff}+1]/3\right)\left(M_{ej}/5\,M_\odot\right)$$
$$\times \left(V_{ej}/5000\text{ km s}^{-1}\right)^{-2}t_7^{-2}, \quad (50)$$

implying that the BH attenuation is significant at very early times. But, since the BH cross section is $\alpha_{em} \simeq 1/137$ times lower than the Thomson cross section, GeV gamma rays allow us to probe subphotospheric regions, i.e., optically thick phases such that $\tau_T^{ej} \gtrsim 1$.

In the small inelasticity limit, a particle loses κ_γ per interaction, so the survival fraction is $(1 - \kappa_\gamma)^{\max[\tau,\tau^2]}$, where $\max[\tau, \tau^2]$ represents the number of scatterings. In the large inelasticity limit, as in the attenuation case, the survival fraction is given by $e^{-\tau}$. Combing the two limits, we approximate the
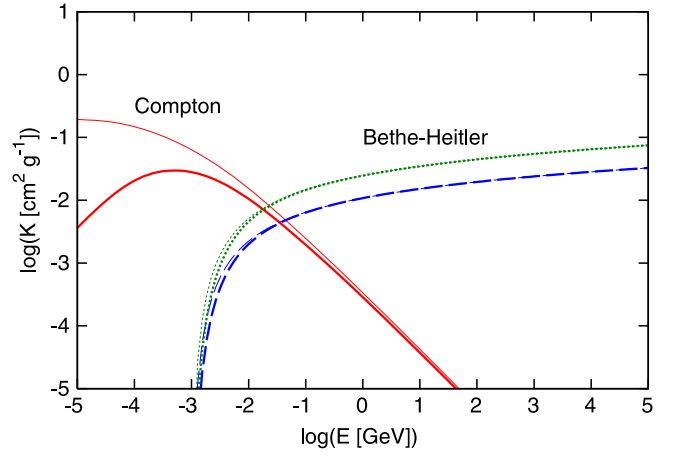
Figure 4. Mass attenuation (thin curves) and mass energy-transfer (thick curves) coefficients as a function of photon energy E. Dashed and dotted curves are for $Z_{eff} = 2.5$ and $Z_{eff} = 7$, respectively.

escape fraction of hard X-rays and gamma rays by

$$f_{esc} = e^{-\tau} + \left(1 - e^{-\tau}\right)(1 - \kappa)^{\max[\tau,\tau^2]}. \quad (51)$$

In Figure 4, we show mass attenuation and mass energy-transfer coefficients. For $M_{ej} = 10\,M_\odot$, we use $Z_{eff} = 2.5$ assuming a typical composition for ejecta of SNe II, whereas we use $Z_{eff} = 7$ for $M_{ej} = 5\,M_\odot$ assuming ejecta are dominated by carbon and oxygen. Different chemical compositions lead to modest influences on attenuated gamma-ray spectra, but our conclusions are not qualitatively altered. In Figure 3, optical depths to Compton and BH pair production processes are shown. Obviously, GeV–TeV gamma rays cannot leave the ejecta until a few months after the explosion. The GeV gamma-ray escape is allowed at

$$t_{\gamma-bo} \simeq 88\text{ days }\left([Z_{eff}+1]/3\right)^{1/2}\left(M_{ej}/5\,M_\odot\right)^{1/2}$$
$$\times \left(V_{ej}/5000\text{ km s}^{-1}\right)^{-1}. \quad (52)$$

In the Thomson limit, the gamma-ray flux at E_{IC}^b for $t \gtrsim t_{em}$ is roughly given by

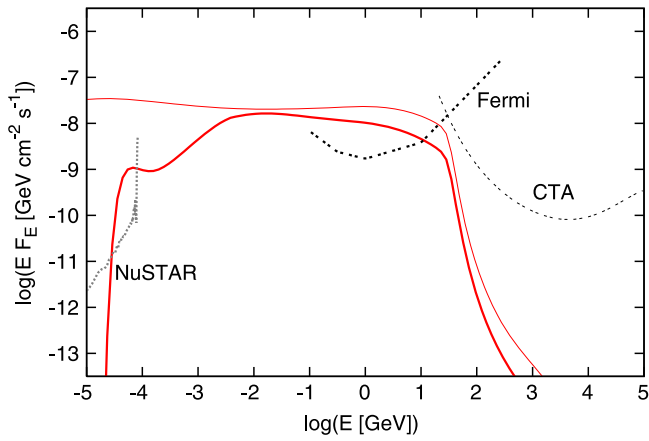$$F_{IC}^b \sim 3.7 \times 10^{-8}\text{ GeV cm}^{-2}\text{ s}^{-1}\,Y(1+Y)^{-1}B_{dip,14}^{-2}\epsilon_e$$
$$\times \left([Z_{eff}+1]/3\right)^{-1}\left(M_{ej}/5\,M_\odot\right)^{-1}\left(V_{ej}/5000\text{ km s}^{-1}\right)^2$$
$$\times (d/16.5\text{ Mpc})^{-2}\left(t/t_{\gamma-bo}\right)^{-2}. \quad (53)$$

Note that the ejecta becomes optically thin to Thomson scattering at

$$t_{HX-bo} \simeq 420\text{ days }\left(2/\mu_e\right)^{1/2}\left(M_{ej}/5\,M_\odot\right)^{1/2}$$
$$\times \left(V_{ej}/5000\text{ km s}^{-1}\right)^{-1}. \quad (54)$$

The synchrotron flux at late times is estimated to be

$$F_{syn}^b \sim 2.6 \times 10^{-12}\text{ erg cm}^{-2}\text{ s}^{-1}\,(1+Y)^{-1}B_{dip,14}^{-2}$$
$$\times \left(2/\mu_e\right)^{-1}\left(M_{ej}/5\,M_\odot\right)^{-1}\left(V_{ej}/5000\text{ km s}^{-1}\right)^2$$
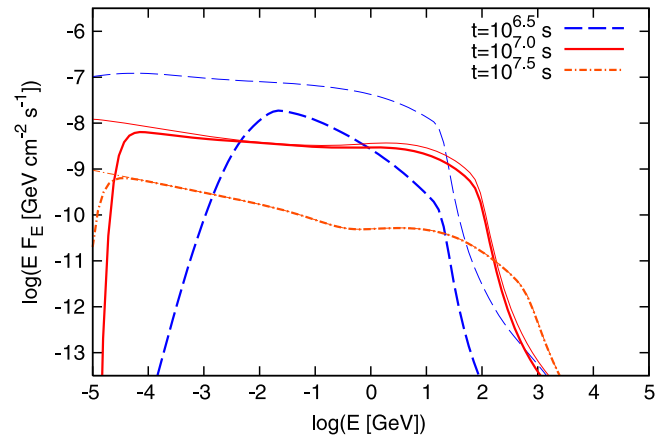$$\times (d/16.5\text{ Mpc})^{-2}(t/t_{HX-bo})^{-2}. \quad (55)$$

Figure 5. High-energy photon spectra of the early PWN embedded in the SN ejecta. The observation time is set to $t = 10^{6.75}$ s $\simeq 65$ days, and the source distance is taken as $d = 16.5$ Mpc. Relevant parameters for dynamics are (P_i, B_{dip}, M_{ej}) = (2 ms, 10^{14} G, 5 $M_\odot$). We show cases with (thick curve) and without (thin curve) matter attenuation. Note that cascades via $\gamma\gamma \rightarrow e^+e^-$ in the emission region are considered. The *Fermi*/LAT sensitivity at the corresponding observation time and *NuSTAR* (10^6 s) and CTA (50 hr) sensitivities (Actis et al. 2011) are also overlaid.

Note that low-energy photons with low κ_γ can escape earlier after they experience multiple scatterings.

3. NUMERICAL RESULTS

We solve Equations (2), (7), (10), (11), (14) and (38) numerically. Then, we approximately take into account matter attenuation in the SN ejecta via Equation (51). Key parameters for dynamics are P_i, B_{dip}, M_{ej} and $\mathcal{E}_{sn}$. Throughout this work, $\mathcal{E}_{sn} = 2 \times 10^{51}$ erg is used. We also consider $M_{ej} = 5M_\odot$ and $M_{ej} = 10\,M_\odot$, which are often suggested from modeling of observed SNe Ibc and II, respectively. To detect X-ray and gamma-ray emission, sufficiently fast-rotating and magnetized NSs are required, so we consider NSs with $P_i \lesssim 10$ ms and $B_{dip} \gtrsim 10^{13}$ G. Other microphysical parameters are treated as sub-parameters, assuming that they are similar to ones suggested in the literature of Galactic PWNe. Motivated by results on the Crab Nebula (Tanaka & Takahara 2010), we assume $\epsilon_B = 0.003$ and $\epsilon_e = 1 - \epsilon_B$, fixing $q_1 = 1.5$, $q_2 = 2.5$ and $\gamma_b = 10^{5.5}$.

In Figure 5, we show hard X-ray and gamma-ray spectra for the millisecond pulsar case with (P_i, B_{dip}, M_{ej}) = (2 ms, 10^{14} G, 5 $M_\odot$). The observation time is set to $t = 10^{6.75}$ s after the explosion. As expected in Equation (37), generated EIC emission has a peak around ~ 10–100 GeV. Although our numerical results and analytical estimates (presented in Section 2.2) come to a reasonable agreement, detailed effects due to energy-dependent cross sections and electromagnetic cascades play roles in making a difference. Two-photon attenuation is still important at early times. One sees that the spectrum below ~ 3 GeV is also softened due to interactions with synchrotron photons (see Figure 3), and that there is a prominent cutoff at ~ 30 GeV, due to SN photons. Furthermore, matter attenuation makes the gamma-ray spectrum even softer. Time evolution of spectra is also shown in Figure 6. Not only various attenuation processes but also the KN effect becomes

**Figure 6.** The same as Figure 5, but at different observation times.
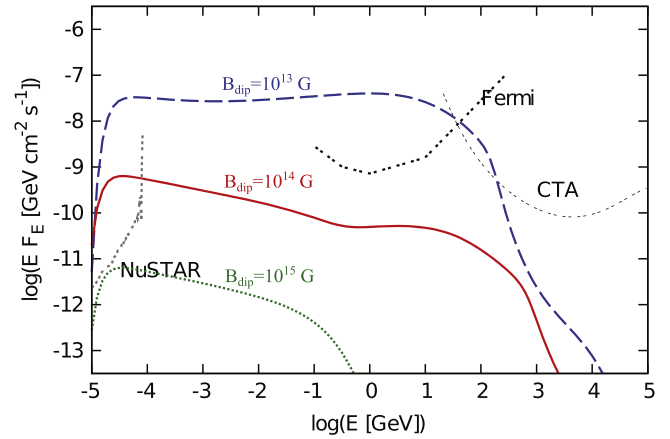
Figure 7. High-energy photon spectra of the early PWN embedded in the SN ejecta for $P_i = 2$ ms at $t = 10^{7.5}$ s $\simeq 316$ days. Different magnetic field strengths are considered. Detections with CTA are possible for $B_{dip} = 10^{13}$ G.

less important in time, and the generated EIC spectrum at ~ 1 yr is described rather by Equation (36). At late times, SN emission becomes so weak that the EIC emission is less important. As a result, the synchrotron component is more prominent, and one sees the synchrotron cutoff expected by Equation (25).

We find that ~ 1–10 GeV gamma rays can be detected by *Fermi* several months after the SN explosion. Here we consider nearby SNe at $d = 16.5$ Mpc, motivated by the possibility that GWs from newborn fast-rotating NSs in the Virgo cluster can be detected by second-generation ground-based GW interferometers (Stella et al. 2005; Dall'Osso et al. 2009). Hard X-ray observations by high-sensitivity satellites such as *NuSTAR* look more promising although follow-up observations are required. As suggested in Figure 7, such pulsar-powered SNe may be detected up to $d \sim 0.1$–1 Gpc, depending on values of B_{dip}.

Note that transients like GRBs and SNe have been potentially interesting targets for imaging atmospheric Cherenkov telescopes and CTA can be especially powerful for that purpose (Kakuwa et al. 2012; Inoue et al. 2013; Bartos et al. 2014). However, for embryonic PWNe, TeV gamma-ray detections may be challenging due to limitation of the maximum energy (see Equation (22)), the KN effect, and two-photon attenuation, although CTA might be able to detect the signal at late times for appropriate values of B_{dip} (see
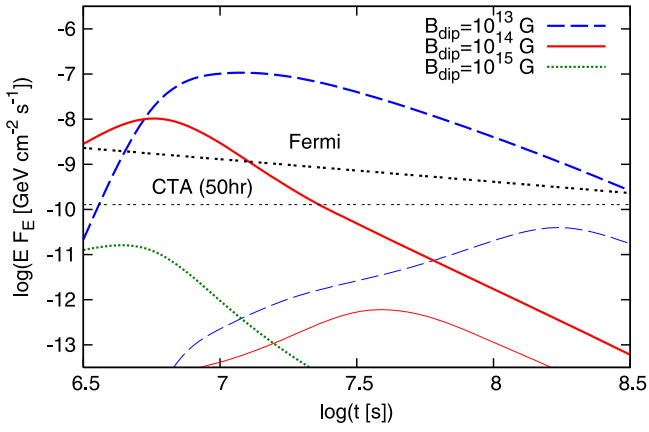
Figure 8. High-energy gamma-ray light curves of the early PWN emission at 1 GeV (thick curves) and 1 TeV (thin curves), for different magnetic field strengths. The *Fermi*/LAT and CTA sensitivities are overlaid. Note that the observation time 50 hr is shorter than t for CTA, while we consider continuous observation for *Fermi*/LAT so the sensitivity changes as $t^{-1/2}$.
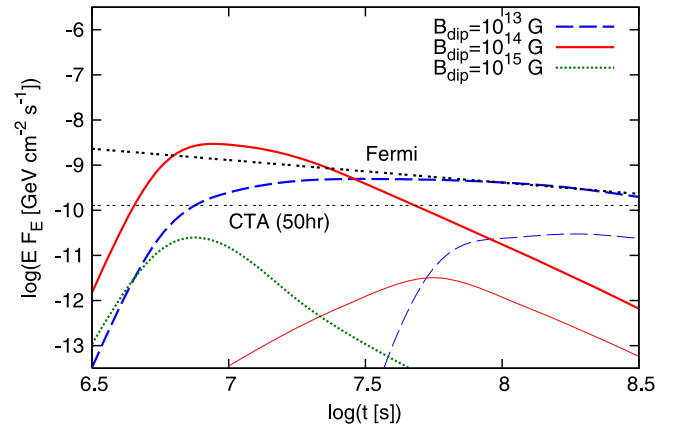

Figure 9. High-energy photon spectra of the early PWN embedded in the SN ejecta for $P_i = 10$ ms at $t = 10^{7.25}$ s $\simeq 206$ days. Different magnetic field strengths are considered.

Figure 7). In Figure 8, we show gamma-ray light curves for different magnetic field strengths. For $P_i \sim 1$–3 ms, it is difficult for *Fermi* to detect GeV gamma rays for magnetic fields with $B_{\rm dip} \gtrsim 10^{14.5}$ G, because the spin-down power rapidly declines at $t \gg t_{\rm em}$ and the target SN photon density also decreases with time. However, hard X-rays are still detectable even for such newborn magnetars, because the synchrotron component decays as t^{-2} and sensitivities of follow-up X-ray observations are better than that of *Fermi*. For a nearby SN at the Virgo cluster, GeV gamma-ray detections are feasible for magnetic fields down to $B_{\rm dip} \lesssim 10^{12}$ G.

Newborn millisecond pulsars have been postulated to explain energetic transients such as super-luminous SNe, hypernovae and GRBs, but it is not clear how newborn NSs acquire such fast rotation. Hence, we consider a more conservative case of $P_i = 10$ ms, which is not far from values inferred for the Crab pulsar and PSR J0537-6910 (Faucher-Giguère & Kaspi 2006). Here, the rotational energy is smaller than the SN explosion energy, so SN dynamics is essentially unaffected by the spin-down power. In Figures 9 and 10, we show spectra and light curves, respectively. Interestingly, we may still expect that GeV gamma rays can be detected for a SN at the Virgo cluster for 10^{13} G $\lesssim B_{\rm dip} \lesssim 10^{14}$ G. Hard X-rays are more promising since the synchrotron signal can be seen up to $d \sim 50$–100 Mpc for $B_{\rm dip} \sim 10^{13}$–10^{14} G, although detections become challenging for sufficiently strong magnetic fields with $B_{\rm dip} \gtrsim 10^{14.5}$ G.

The core-collapse SN rates within 20 Mpc and within 50 Mpc are estimated to be ~ 3 and ~ 50 yr^{-1}, respectively. However, we expect that only a fraction of SNe can leave NSs with fast rotation. The most optimistic case is motivated by the dynamo hypothesis for magnetars, which requires fast rotation. Since the magnetar fraction is believed to be $\sim 10\%$ of all NSs, the probability to expect high-energy counterparts may not be so low. Hypernovae or trans-relativistic SNe associated with low-luminosity GRBs, which are often thought to be engine-driven SNe, could come from fast-rotating pulsars, and their rates are typically a few percent of the core-collapse SN rate. If we assume that 2% of SNe lead to such SNe, their rate within 50 Mpc is estimated to be ~ 1 yr^{-1}, which is encouraging. For
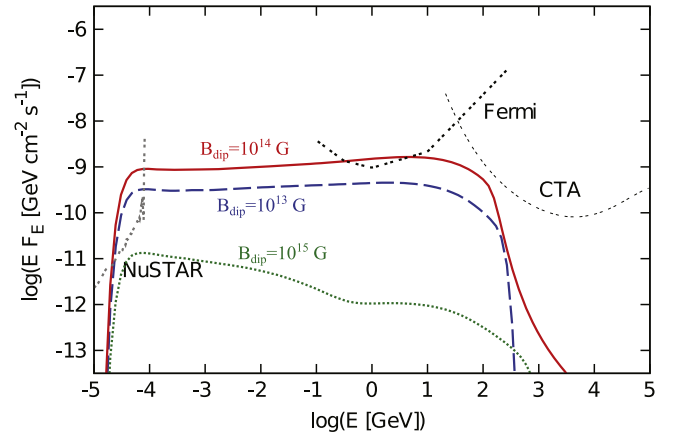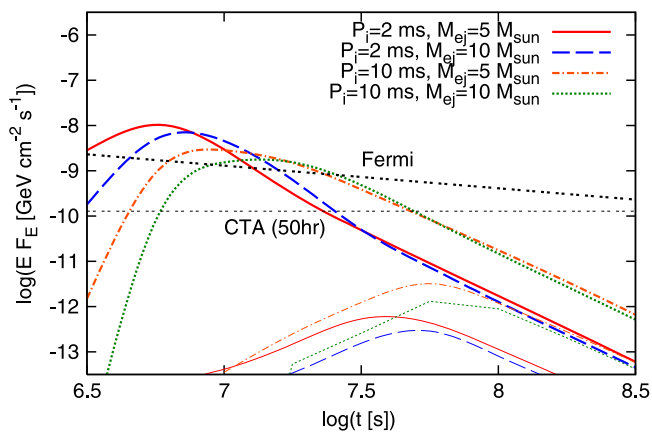

Figure 10. The same as Figure 8, but for $P_i = 10$ ms.
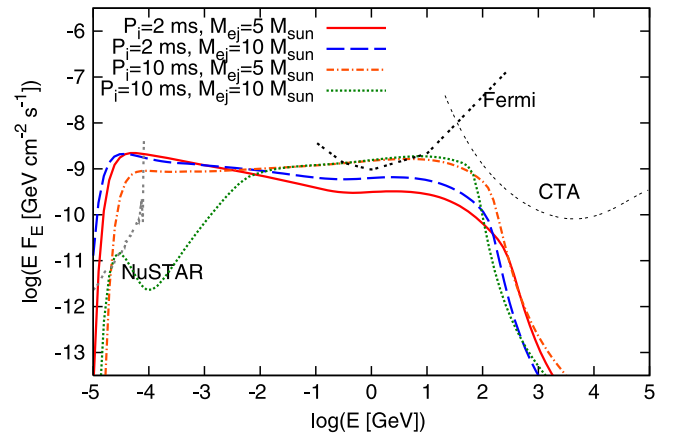
Figure 11. High-energy photon spectra of the early PWN embedded in the SN ejecta for different values of P_i and $M_{\rm ej}$. The observation time is set to $t = 10^{7.25}$ s $\simeq 206$ days.

GeV gamma rays, we suggest that individual searches and stacking analyses for super-luminous SNe and hypernovae may be more promising. In particular, in view of modeling of light curves and energetics, hydrogen-poor super-luminous SNe are interesting targets (Quimby et al. 2011; Vreeswijk et al. 2014), and finding evidence for gamma rays from these SNe can support the hypothesis that they are driven by newborn pulsars.

Figure 12. The same as Figure 8, but for different values of P_i and M_{ej}.

In Figures 11 and 12, we show the dependence on M_{ej}. Obviously, for the same values of B_{dip} and P_i, escape of photons is more difficult for larger M_{ej}. However, after hard X-rays or gamma rays break out (i.e., $\tau_T^{ej} \lesssim 1$ or $\tau_{BH}^{ej} \lesssim 1$), one sees that the dependence on M_{ej} is quite modest. This also implies that the most important parameters in our model are B_{dip} and P_i.

4. DISCUSSION AND SUMMARY

We showed that high-energy emission from embryonic PWNe provides a useful probe of particle acceleration at very early stages of SNe leaving a fast-rotating NS remnant. We described analytical spectra of generated IC emission, taking into account the KN effect that is important above ~10–100 GeV. Initially, two-photon attenuation prevents gamma rays from leaving the PWN and further attenuation in the SN ejecta is unavoidable. Although analytical estimates and numerical calculations reach a reasonable agreement, details of microphysical processes, including electromagnetic cascades, affect the resulting gamma-ray spectra. After several months, the PWN itself becomes transparent to gamma rays, and GeV gamma rays break out before optical photons and X-rays escape.

In this work, we focused on presenting detailed spectra and light curves. We will carry out a parameter survey on the detectability in the plane of B_{dip}, P_i and d in future. Nevertheless, here we briefly discuss detectability in a typical scenario to provide a picture of the prospects of current and future observations. If such a SN in a galaxy in the Virgo cluster leaves a NS with $P_i = 2$ ms, gamma rays can be detected by *Fermi* for 10^{12} G $\lesssim B_{dip} \lesssim 10^{14.5}$ G. For $P_i = 10$ ms, detections are possible in narrower ranges 10^{13} G $\lesssim B_{dip} \lesssim 10^{14}$ G, and become more difficult for larger values of P_i. Even though detections of IC emission from a single source with GeV gamma rays are limited to nearby sources and the PWN emission can be seen by *Fermi* up to $d \lesssim 40$ Mpc for $B_{dip} \sim 10^{14}$ G, we found that gamma rays can still provide us with useful counterparts of GW emission from newborn NSs. In addition, to test the possibility that super-luminous SNe are driven by fast-rotating NSs (cf. Murase et al. 2011a), individual and stacking analyses on transients with timescales of months to years can also be useful. We also showed that observations of non-thermal synchrotron emission at hard X-rays can be more powerful to identify pulsar-aided

SNe, although dedicated follow-up observations (e.g., by *NuSTAR*) are required. A newborn NS with $P_i = 2$ ms at $d = 16.5$ Mpc can be detected for reasonable magnetic fields $10^{11.5}$ G $\lesssim B_{dip} \lesssim 10^{15}$ G with observation time $\sim10^5$–10^6 s. For $P_i = 10$ ms, 10^{12} G $\lesssim B_{dip} \lesssim 10^{14.5}$ G is needed, and *NuSTAR*-like detectors can detect a source up to $d \sim 80$ Mpc for $B_{dip} \sim 10^{14}$ G. It is likely that only a fraction of core-collapse SNe can leave NSs with $P_i \lesssim 10$ ms. Assuming that a fraction f_r of NSs can be rapidly rotating and we can detect all SNe in the nearby universe with surveys such as ASAS-SN,[17] the rate to have such events within d may be ~0.5 yr^{-1} $f_{r,-2}$ $(d/50$ Mpc$)^3$, which is in the interesting range.

One may expect not only high-energy gamma rays but also high-energy neutrinos as GW counterparts. Neutrino detections from newborn NSs are also promising for nearby SNe. Until the proto-PNS becomes transparent to neutrinos, baryons including neutrons may be loaded into the proto-NS wind via MeV neutrinos. Neutrons that are initially coupled to ions should be magnetically accelerated together. Then, dissipation of relativistic neutron flows inevitably leads to GeV–TeV neutrino production. Since the baryon loading is not small at early stages, ion acceleration before and/or at the termination shock could also be efficient, where TeV or higher-energy neutrino production is possible (Murase et al. 2014). At later times after the proto-PNS becomes transparent to neutrinos (i.e., $t \gg 10$–100 s), it would be more natural that the wind is largely dominated by electrons and positrons. But, it has also been speculated that dissipation in the current sheet may lead to ion acceleration and observed cosmic rays can be explained (Ostriker & Gunn 1969; Arons 2003; Fang et al. 2013b). If this is the case, EeV neutrinos provide a powerful test of this hypothesis (Murase et al. 2009; Fang et al. 2013a).

Our assumption is that phenomenology of Galactic PWNe can be extrapolated to early PWNe. The detectability is sensitive to B_{dip} and P_i and it is theoretically unclear how such fast-spinning NSs are born. Indeed, although hard X-ray observations at early times are more relevant for sufficiently large B_{dip}, non-observations in the soft X-ray range suggest that only a fraction of NSs can be born with fast rotation (Perna et al. 2008). There is no evidence for such a pulsar in SN 1987 A. On the other hand, high-energy emission is detectable even for non-extreme values of P_i and B_{dip} as in the Crab pulsar, and possible candidates have been reported for historical SNe in X-rays (Soria & Perna 2008). We encourage individual and stacking searches using *Fermi* data. Although the high fraction of such events has apparently been constrained by non-observations, some could be unidentified transients. Importantly, successful detections should allow us to study the beginning of particle acceleration in PWNe. Magnetic dissipation and subsequent particle acceleration mechanisms have been long-standing problems (see, e.g., Hoshino et al. 1992; Kirk 2010; Sironi & Spitkovsky 2011; Arons 2012, and references therein). High-energy signals would imply that the Poynting energy is efficiently converted into the particle energy, and one can put constraints on ϵ_B by observing the IC component. Also, if possible, measurements of the spectral shape would be useful for constraining η, γ_b (or $\mu_\pm$) and investigating physical connection to Galactic PWNe.

If strong non-thermal signatures of embryonic PWNe are detected for super-luminous SNe or hypernovae, it can support

---

[17] http://www.astronomy.ohio-state.edu/assassin/index.shtml

that fast-rotating pulsars play a role in SN emission or even its dynamics. Note that there are several competing scenarios for super-luminous SNe, including the interaction-powered SN scenario and pair-instability SN scenario. Interaction-powered SNe have been suggested to be sources of hadronic GeV–TeV gamma rays and TeV–PeV neutrinos (Murase et al. 2011a). Properties of non-thermal spectra should be different, so discrimination between the two scenarios is possible. In the interaction-powered SN scenario, non-thermal gamma-ray and neutrino emission becomes prominent around shock breakout from optically thick circumstellar material (although the reverse-shock neutrino emission could be expected before photons escape), and thermal X-ray and narrow width hydrogen line emission accompanies it (e.g., Ofek et al. 2013, 2014; Margutti et al. 2014). Although non-thermal hard X-rays are expected as well (Murase et al. 2011a), after the shock breakout and GeV–TeV gamma rays escape, their flux is lower than the gamma-ray flux. On the other hand, in the pulsar-aided SN scenario, synchrotron X-rays are stronger than IC gamma rays. We suggest that, if pulsars are embedded in the ejecta, high-energy emission is promising especially for hydrogen-poor SNe (although it may also be caused by collisions with circumstellar material) (Quimby et al. 2011; Benetti et al. 2014; Chen et al. 2014; Nicholl et al. 2014; Vreeswijk et al. 2014). Also, for normal luminosity SNe, the ratio of TeV emission to GeV emission is lower than that in the interaction-powered SN scenario where gamma rays are hadronically produced. Although GRBs are not considered in this work, magnetic dissipation and particle acceleration might occur even when the proto-NS wind forms Poynting-dominated jet-like outflows. We note that shallow-decay afterglow emission is often explained by energy injection via the magnetar spin down (e.g., Metzger et al. 2011), and that the observed X-ray emission, which could be associated with the GW emission (Corsi & Mészáros 2009), can be attributed to synchrotron emission from leptons accelerated via internal magnetic dissipation (Ghisellini et al. 2007; Metzger et al. 2011; Murase et al. 2011b). We also suggest that magnetic dissipation in embryonic PWNe may be relevant for the long-lasting X-ray emission (Murase et al. 2011b).

Our calculations can also be applied to high-energy counterparts of short GRBs and double NS mergers. A pulsar-aided mechanism could also be relevant in double NS mergers given that the equation of state is quite stiff (Kisaka et al. 2014), where GeV–TeV gamma rays and X-rays from embryonic PWNe can be useful as a signature of this scenario.

REFERENCES

Acernese, F., Agathos, M., Agatsuma, K., et al. 2014, arXIv:1408.3978
Actis, M., Agnetta, G., Aharonian, F., et al. 2011, ExA, 32, 193
Arcavi, I., Gal-Yam, A., Kasliwal, M. M., et al. 2010, ApJ, 721, 777
Arons, J. 2003, ApJ, 589, 871
Arons, J. 2012, SSRv, 173, 341
Atoyan, A. M., & Aharonian, F. A. 1996, MNRAS, 278, 525
Bartos, I., Brady, P., & Márka, S. 2013, CQGra, 30, 123001
Bartos, I., Veres, P., Nieto, D., et al. 2014, MNRAS, 443, 738
Begelman, M. C. 1998, ApJ, 493, 291
Benetti, S., Nicholl, M., Cappellaro, E., et al. 2014, MNRAS, 441, 289
Blackman, E. G., & Yi, I. 1998, ApJL, 498, L31
Buccciantini, N., Quataert, E., Arons, J., Metzger, B. D., & Thompson, T. A. 2007, MNRAS, 380, 1541
Buccciantini, N., Quataert, E., Arons, J., Metzger, B. D., & Thompson, T. A. 2008, MNRAS, 383, L25
Cerutti, B., Philippov, A., Parfrey, K., & Spitkovsky, A. 2014, arXiv:1410.3757
Chen, T.-W., Smartt, S. J., Jerkstrand, A., et al. 2014, arXiv:1409.7728
Chevalier, R. A. 1977, in Supernovae, ed. D. N. Schramm (Astrophysics and Space Science Library, Vol. 66; Berlin: Springer), 53
Chevalier, R. A., & Fransson, C. 1992, ApJ, 395, 540
Chodorowski, M. J., Zdziarski, A. A., & Sikora, M. 1992, ApJ, 400, 181
Corsi, A., & Mészáros, P. 2009, ApJ, 702, 1171
Cutler, C. 2002, PhRvD, 66, 084025
Dai, Z. G., & Lu, T. 1998, A&A, 333, L87
Dall'Osso, S., Shore, S. N., & Stella, L. 2009, MNRAS, 398, 1869
de Jager, O. C., Harding, A. K., Michelson, P. F., et al. 1996, ApJ, 457, 253
Dermer, C. D., Murase, K., & Takami, H. 2012, ApJ, 755, 147
Duncan, R. C., & Thompson, C. 1992, ApJL, 392, L9
Fang, K., Kotera, K., Murase, K., & Olinto, A. V. 2013a, arXiv:1311.2044
Fang, K., Kotera, K., & Olinto, A. V. 2013b, JCAP, 3, 10
Faucher-Giguère, C.-A., & Kaspi, V. M. 2006, ApJ, 643, 332
Gaensler, B. M., & Slane, P. O. 2006, ARA&A, 44, 17
Gaisser, T. K., Stanev, T., & Harding, A. 1987, Natur, 329, 314
Gal-Yam, A. 2012, Sci, 337, 927
Ghisellini, G., Ghirlanda, G., Nava, L., & Firmani, C. 2007, ApJL, 658, L75
Goldreich, P., & Julian, W. H. 1969, ApJ, 157, 869
Gruzinov, A. 2005, PhRvL, 94, 021101
Harry, G. M., & LIGO Scientific Collaboration 2010, CQGra, 27, 084006
Hoshino, M., Arons, J., Gallant, Y. A., & Langdon, A. B. 1992, ApJ, 390, 454
Inoue, S., Granot, J., O'Brien, P. T., et al. 2013, APh, 43, 252
Inserra, C., Smartt, S. J., Jerkstrand, A., et al. 2013, ApJ, 770, 128
Kakuwa, J., Murase, K., Toma, K., et al. 2012, MNRAS, 425, 514
Kasen, D., & Bildsten, L. 2010, ApJ, 717, 245
Kennel, C. F., & Coroniti, F. V. 1984, ApJ, 283, 694
Kirk, J. G. 2010, PPCF, 52, 124029
Kisaka, S., Ioka, K., & Takami, H. 2014, arXiv:1410.0966
Kokkotas, K. D. 2008, in Reviews in Modern Astronomy, Vol. 20, Cosmic Matter, ed. S. Röser (Berlin: Springer), 140
Komissarov, S. S., & Barkov, M. V. 2007, MNRAS, 382, 1029
Kotera, K., Phinney, E. S., & Olinto, A. V. 2013, MNRAS, 432, 3228
Lattimer, J. M., & Prakash, M. 2001, ApJ, 550, 426
Lyubarsky, Y., & Kirk, J. G. 2001, ApJ, 547, 437
Margutti, R., Milisavljevic, D., Soderberg, A. M., et al. 2014, ApJ, 780, 21
McCrum, M., Smartt, S. J., Kotak, R., et al. 2014, MNRAS, 437, 656
Medvedev, A. S., & Poutanen, J. 2013, MNRAS, 431, 2690
Metzger, B. D., Giannios, D., Thompson, T. A., Bucciantini, N., & Quataert, E. 2011, MNRAS, 413, 2031
Metzger, B. D., Vurm, I., Hascoet, R., & Beloborodov, A. M. 2014, MNRAS, 437, 703
Murase, K., Dasgupta, B., & Thompson, T. A. 2014, PhRvD, 89, 043012
Murase, K., Mészáros, P., & Zhang, B. 2009, PhRvD, 79, 103001
Murase, K., Thompson, T. A., Lacki, B. C., & Beacom, J. F. 2011a, PhRvD, 84, 043003
Murase, K., Toma, K., Yamazaki, R., & Mészáros, P. 2011b, ApJ, 732, 77
Murase, K., Toma, K., Yamazaki, R., Nagataki, S., & Ioka, K. 2010, MNRAS, 402, L54
Nicholl, M., Smartt, S. J., Jerkstrand, A., et al. 2013, Natur, 502, 346
Nicholl, M., Smartt, S. J., Jerkstrand, A., et al. 2014, MNRAS, 444, 2096
Ofek, E. O., Fox, D., Cenko, S. B., et al. 2013, ApJ, 763, 42
Ofek, E. O., Zoglauer, A., Boggs, S. E., et al. 2014, ApJ, 781, 42
Ostriker, J. P., & Gunn, J. E. 1969, ApJ, 157, 1395

Ostriker, J. P., & Gunn, J. E. 1971, ApJL, 164, L95
Perna, R., Soria, R., Pooley, D., & Stella, L. 2008, MNRAS, 384, 1638
Porth, O., Komissarov, S. S., & Keppens, R. 2014, MNRAS, 438, 278
Quimby, R. M., Kulkarni, S. R., Kasliwal, M. M., et al. 2011, Natur, 474, 487
Rees, M. J., & Gunn, J. E. 1974, MNRAS, 167, 1
Sironi, L., & Spitkovsky, A. 2011, ApJ, 741, 39
Smith, N., Li, W., Filippenko, A. V., & Chornock, R. 2011, MNRAS, 412, 1522
Somiya, K., & KAGRA Collaboration 2012, CQGra, 29, 124007
Soria, R., & Perna, R. 2008, ApJ, 683, 767
Spitkovsky, A. 2006, ApJL, 648, L51
Stella, L., Dall'Osso, S., Israel, G. L., & Vecchio, A. 2005, ApJL, 634, L165

Tanaka, S. J., & Takahara, F. 2010, ApJ, 715, 1248
Tanaka, S. J., & Takahara, F. 2013, MNRAS, 429, 2945
Tchekhovskoy, A., Spitkovsky, A., & Li, J. G. 2013, MNRAS, 435, L1
Thompson, T. A., Chang, P., & Quataert, E. 2004, ApJ, 611, 380
Usov, V. V. 1992, Natur, 357, 472
Verezinskii, V. S., & Prilutskii, O. F. 1978, A&A, 66, 325
Volonteri, M., & Perna, R. 2005, MNRAS, 358, 913
Vreeswijk, P. M., Savaglio, S., Gal-Yam, A., et al. 2014, arXiv:1409.8287
Wheeler, J. C., Yi, I., Höflich, P., & Wang, L. 2000, ApJ, 537, 810
Woosley, S. E. 2010, ApJL, 719, L204
Zhang, B., & Mészáros, P. 2001, ApJL, 552, L35